Letter

Transient nuclear inversion by x-ray free electron laser in a tapered x-ray waveguide

Yu-Hsueh Chen,[1,2] Po-Han Lin,[1] Guan-Ying Wang,[1] Adriana Pálffy,[3,4,2,*] and Wen-Te Liao[1,2,5,6,†]

[1]*Department of Physics, National Central University, Taoyuan City 32001, Taiwan*

[2]*Max-Planck-Institut für Kernphysik, Saupfercheckweg 1, D-69117 Heidelberg, Germany*

[3]*Institute of Theoretical Physics and Astrophysics, University of Würzburg, Am Hubland, 97074 Würzburg, Germany*

[4]*Department of Physics, Friedrich-Alexander-Universität Erlangen-Nürnberg, D-91058, Erlangen, Germany*

[5]*Physics Division, National Center for Theoretical Sciences, Taipei 10617, Taiwan*

[6]*Center for Quantum Technology, Hsinchu 30013, Taiwan*

(Received 5 July 2021; accepted 16 June 2022; published 11 July 2022)

The enhancement of x-ray-matter interaction by guiding and focusing radiation from x-ray free electron lasers is investigated theoretically. We show that elliptical waveguides using a cladding material with a high atomic number, such as platinum, can maintain an x-ray intensity of up to three orders of magnitude larger than in free space. This feature can be used to place a nuclear sample in the waveguide focal area and drive nuclear Mössbauer transitions up to transient nuclear population inversion. The latter is a long-standing goal related to gamma-ray lasers or nuclear state population control for energy storage. We show that inverted nuclei numbers of up to approximately 2×10^5 are achievable in the realistic region of longitudinal x-ray-free-electron-laser coherence time $\leqslant 10$ fs. Our results anticipate the important role of tapered x-ray waveguides and strategically embedded samples in the field of x-ray quantum optics.

DOI: 10.1103/PhysRevResearch.4.L032007

Introduction. The first x-ray free electron laser (XFEL) facilities [1,2] open new avenues for the interaction of high-frequency lasers with atoms, molecules, or even atomic nuclei which can be resonant to x-ray frequencies. However, even intense XFEL radiation is still far from achieving substantial nuclear excitation or population inversion [3,4]. Historically, the latter has been mentioned in the context of gamma-ray lasers, but so far never achieved [5]. Efficient nuclear population control would also be desirable for a safe and clean energy storage solution based on long-lived nuclear excited states, i.e., isomers [6]. In addition, transient nuclear inversion paves the way towards a new type of strong XFEL Mössbauer source [7,8] whose polarization and wavefront are much easier to control via magnetic switching [9,10] or mechanical vibration [11,12] compared to XFEL wavefronts.

So far, nuclear condensed matter [9,11,13–19] and x-ray quantum optics experiments [3,12,20–27] drove Mössbauer transitions in the weak-excitation, single-photon regime at synchrotrons. The more desirable nonlinear regime, which would allow for photon-photon interactions in the x-ray frequency range, could not be accessed thus far. The corresponding strong x-ray-nuclear interaction also requires, apart from increased brilliance, enhancement of nuclear-x-ray interactions in cavities and waveguides (WG). Grazing incidence x-ray cavities with embedded Mössbauer nuclei [20–24,26,28] or normal-incidence cavities based on diamond mirrors [29,30] are lossy and cannot match performances at optical frequencies. Theoretical predictions on nuclear excitation in x-ray thin-film cavities have placed high requirements on the x-ray photon number per pulse for population inversion [31]. The nanofocusing capabilities of tapered capillary WG on the other hand was demonstrated nearly three decades ago [32] with continuous progress ever since [33–42].

In this Letter, we investigate the prospects of tapered x-ray WG for efficient nuclear excitation towards the non-linear regime with an XFEL. A tapered WG presents a gradual narrowing structure of the cladding material and focuses x rays [36,39,40,43–45], boosting their capability of resonantly interacting with and exciting atomic nuclei. We show that elliptical waveguides (EWG) using a cladding material such as platinum can maintain an x-ray intensity up to three orders of magnitude larger than its input. Based on this enhancement, by placing a Mössbauer nuclear sample at the focal area, transient nuclear population inversion can be reached for realistic XFEL parameters. This nuclear population inversion can pave the way towards nonlinear x-ray effects, release on demand of nuclear energy from isomers or secondary graser-like x-ray sources. Furthermore, our results design a tool for XFEL nanofocusing which will be useful for a plethora of fields, starting from imaging, holography, condensed matter physics, and in particular nuclear physics or energy storage, opening additional physics cases at XFEL facilities.

*adriana.palffy-buss@physik.uni-wuerzburg.de

†wente.liao@g.ncu.edu.tw

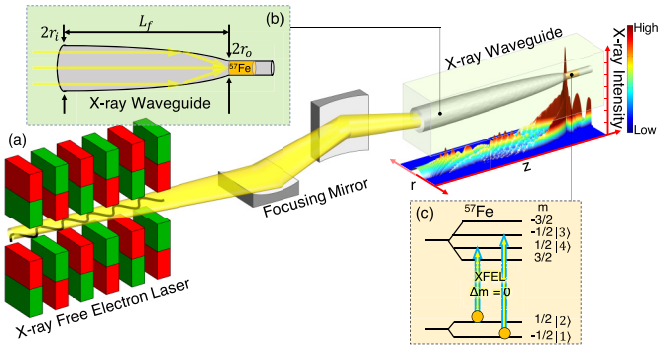

FIG. 1. (a) A nuclear sample (yellow cylinder) is placed at the WG focal point (sketch not to scale). The intrawaveguide x-ray intensity is depicted below. (b) A bottle-like tapered WG with input radius r_i, output radius r_o and focusing length L_f. (c) ^{57}Fe nuclear level scheme. A linearly polarized XFEL pulse (blue arrows) drives the two $\Delta m = 0$ transitions. We label the two ground states with $|1\rangle$, $|2\rangle$ and the relevant excited states with $|3\rangle$ and $|4\rangle$, respectively.

Figure 1(a) illustrates our setup. The XFEL is prefocused by, e.g., Kirkpatrick-Baez focusing mirrors which have reached sub-μm capabilities [46]. A nuclear sample is directly embedded in the WG focal area. A tapered WG is described by the focusing length L_f, the input (output) port radius r_i (r_o), the cladding material, and the cladding-vacuum interface geometry illustrated in Fig. 1(b). Nuclear resonance fluorescence will be emitted in WG modes, leading to directional emission relevant for downstream detection and applications. As a main example we consider a sample of ^{57}Fe Mössbauer nuclei, which have a 14.4 keV nuclear transition of magnetic dipole multipolarity. Similar Mössbauer transitions with ground (excited) state nuclear spin $I_g = 1/2$ ($I_e = 3/2$) in ^{133}Ba, ^{187}Os, and ^{169}Tm are also addressed, see Table I. In the chosen setup geometry, the pulse drives the two transitions $\Delta m = m_e - m_g = 0$, where m_e (m_g) are the corresponding spin projections.

Theoretical model. We consider a linearly polarized and fully coherent XFEL pulse. Later on we use the partial-coherence method to numerically simulate the self-amplified spontaneous emission (SASE) XFEL pulse structure [49]. Fully coherent x-ray pulses can be delivered by seeded XFELs [50–55], an XFEL oscillator (XFELO) [56–61], or their combination [62,63]. The nuclear dynamics is described by Bloch equations for the density matrix ρ [64,65],

$$\partial_t \rho_{gg} = \left(\frac{\alpha}{1+\alpha}\right)\Gamma_s \rho_{ee} + \frac{i}{2}(\Omega^* \rho_{eg} - \Omega \rho_{eg}^*), \quad (1)$$

$$\partial_t \rho_{eg} = -\left(\frac{\alpha}{1+\alpha}\right)\frac{\Gamma_s}{2}\rho_{eg} - \frac{i}{2}\Omega(\rho_{ee} - \rho_{gg}), \quad (2)$$

$$\partial_t \rho_{ee} = -\left(\frac{\alpha}{1+\alpha}\right)\Gamma_s \rho_{ee} - \frac{i}{2}(\Omega^* \rho_{eg} - \Omega \rho_{eg}^*), \quad (3)$$

where the subscripts $(e, g) = (3, 1)$ or $(4, 2)$ label the nuclear states as illustrated in Fig. 1(c). In Eqs. (1)–(3), the incoherent decay is attributed to the internal conversion rate $\frac{\alpha}{1+\alpha}\Gamma_s$ which cannot be suppressed by the WG, where Γ_s is the spontaneous radiative decay rate and α the internal conversion coefficient. Following Refs. [64,66–68], we define the Rabi frequency $\Omega = \Pi E/\hbar$, where $E = |\mathbf{E}|$ is the electric field strength modulus and $\Pi = 4a\mu\sqrt{1.79(2I_e+1)\pi B(M1)}/3$ the nuclear matrix element with $\mu = 0.105\, e$ fm the nuclear magneton, e the electron charge, $I_e = 3/2$ the excited state spin, $a = \sqrt{2/3}$ the corresponding Clebsch-Gordan coefficient, and $B(M1)$ the reduced transition probability for the magnetic dipole nuclear transition, respectively. The Maxwell wave equation describes the x-ray propagation [68–71]:

$$\left(\partial_x^2 + \partial_y^2\right)E + 2ik\left(\partial_z + \frac{1}{c}\partial_t\right)E + k^2[n(\mathbf{r})^2 - 1]E = -\left[\frac{8\pi\hbar\Gamma_s N(\mathbf{r})}{\Pi k}\frac{2I_e+1}{2I_g+1}\frac{f_{lm}}{\alpha+1}\right](\rho_{31} + \rho_{42}). \quad (4)$$

Here, k is the x-ray wave vector and c denotes the speed of light in vacuum. $N(\mathbf{r})$ is the nuclear particle number density distribution, f_{lm} the Lamb-Mössbauer factor, and $n(\mathbf{r}) = 1 - \delta(\mathbf{r}) + i\beta(\mathbf{r})$ the electronic index of refraction [40,70,72], respectively. The position in space $\mathbf{r}$ determines the WG material, with the index of refraction values for Pt, Si or the nuclei of interest presented in Table I. We numerically solve Eqs. (1)–(4) in cylindrical coordinates (r, z) with the initial conditions $\rho_{33}(r, z, 0) = \rho_{44}(r, z, 0) = \rho_{31}(r, z, 0) = \rho_{42}(r, z, 0) = E(r, z, 0) = 0$, $\rho_{11}(r, z, 0) = \rho_{22}(r, z, 0) = 1/2$, and the boundary condition [66,67,73] at $z = 0$

$$E(r, 0, t) = \sqrt{\frac{n_p E_t \sqrt{2}}{c\epsilon_0 \sigma^2 \tau \sqrt{\pi^3}}} \exp\left(-\frac{r^2}{\sigma^2} - \frac{(t - t_c)^2}{4\tau^2}\right). \quad (5)$$

Here, ϵ_0 is the vacuum permittivity, $t_c = 250$ fs is the XFEL peak time, and E_t the nuclear transition energy, respectively. Furthermore, n_p, σ, and τ are the photon number per pulse, beam waist (after the first focusing mirror), and pulse duration

TABLE I. For each nucleus with atomic mass number A we present the nuclear transition energy E_t, the number density N, the calculated Lamb-Mössbauer factor f_{lm}, the reduced nuclear transition probability $B(M1)$ in Weisskopf units (W.u.), the internal conversion coefficient α and the spontaneous radiative rate Γ_s. The last six columns give the x-ray index of refraction $n = 1 - \delta + i\beta$ for WG materials [47,48].

							$\delta(10^{-6})$			$\beta(10^{-7})$		
$^A X$	E_t (keV)	N (10^{28}/m^3)	f_{lm}	$B(M1)$ (W.u.)	α	Γ_s (MHz)	$^A X$	Pt	Si	$^A X$	Pt	Si
^{169}Tm	8.410	3.32	0.84	0.0342	263	169	19.0	47.5	6.94	13.4	43.7	1.46
^{187}Os	9.756	7.15	0.96	0.0260	280	291	36.0	34.7	5.14	24.6	25.7	0.81
^{133}Ba	12.327	1.54	0.38	0.0230	69.5	99.0	3.93	21.2	3.21	3.10	28	0.32
^{57}Fe	14.413	8.49	0.80	0.0078	8.65	7.05	7.44	16.1	2.34	3.39	24.9	0.17

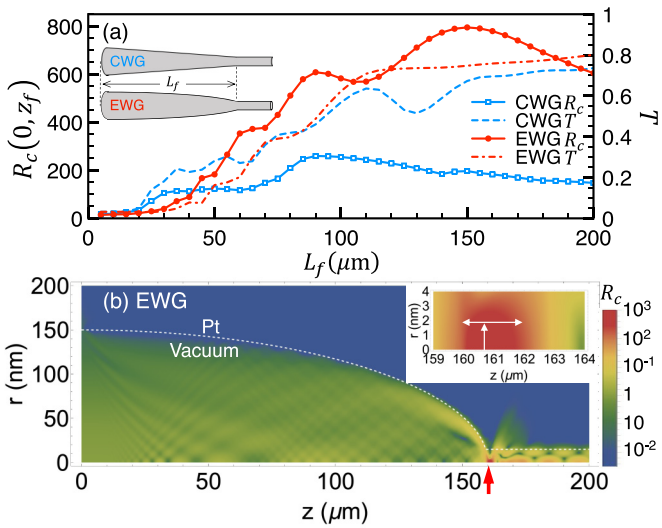

FIG. 2. (a) Intrawaveguide x-ray concentration ratio $R_c(r = 0, z)$ (left vertical axis) and transmission T (right vertical axis) of the CWG (blue empty squares and blue dashed line) and EWG (red dots and red dashed-dotted line) with common parameters (r_i, L_f, r_o, σ) = (150 nm, 160 μm, 15 nm, 120 nm). (b) Contour plots of $R_c(r, z)$ for a Pt-cladding EWG. The red-upward arrow pinpoints the EWG focal point. White dashed lines indicate the platinum cladding and vacuum interface. The inset zooms in on the WG focal point. The white horizontal (vertical) arrow indicates the intrawaveguide Rayleigh length (focal spot size).

of the input XFEL pulse, respectively. Notably, the use of Eq. (4) and Eq. (5) is more realistic than the effective intensity approach [74] and renders stronger nuclear excitation. We define the intrawaveguide x-ray concentration ratio R_c and the focal transmission T to characterize the present WGs

$$R_c(r, z) = |E(r, z)|^2/|E(0, 0)|^2, \tag{6}$$

$$T = \left(\int_0^{r_o} |E(r, z_f)|^2 r dr\right) \Big/ \left(\int_0^{r_i} |E(r, 0)|^2 r dr\right). \tag{7}$$

R_c depicts the degree of x-ray focusing and the spatial intensity distribution, and T reveals the throughput rate at the focus $z = z_f$. Numerically, the cladding term dominates over the nuclear coherences in Eq. (4), which allows for the steady-state calculation, i.e., solving Eq. (4) without nuclear coherence and temporal derivative terms [37,70]. By calculating the steady-state R_c [37,70], we obtain the XFEL pulse area and the nuclear inversion $I_v = \rho_{33} + \rho_{44} - \rho_{11} - \rho_{22}$ [74]

$$I_v(r, z) = -\cos\left[2\frac{\Pi}{\sigma\hbar}\sqrt{\frac{\tau n_p R_c(r, z) E_t \sqrt{2}}{c\epsilon_0\sqrt{\pi}}}\right]. \tag{8}$$

The number of inverted nuclei can be calculated as $\int_{I_v>0} N(\mathbf{r})[\rho_{33}(\mathbf{r}) + \rho_{44}(\mathbf{r})]d^3r$. In the following we refer to the active volume as the region where $I_v > 0$.

Focusing x-rays in a tapered waveguide. In Fig. 2 we present our steady-state solutions of Eq. (4) with only Pt cladding. We compare an EWG with a conical waveguide (CWG), whose cladding-vacuum interface is a cone, both sharing the parameters (r_i, r_o, σ) = (150 nm, 15 nm, 120 nm). An EWG with $r = r_i\sqrt{(1 - (z/L_f)^2)}$ will guide x rays from one focal point to another via only a single reflection on the interface, reducing photon loss. In practice, ellipsoidal glass capillaries have been used as condensers for x-ray microscopes [34]. X rays experience focusing for $z \leqslant 160$ μm in both WGs, but behave very differently for $z > 160$ μm. Fig. 2(a) shows the L_f-dependent focal $R_c(0, z_f)$ and T values. The EWG transmission becomes higher than that of CWG when $L_f \geqslant 80$ μm, and the gap between the two R_c curves is increasing for $L_f > 40$ μm. In contrast to the maximum CWG $R_c \approx 250$ at $L_f = 90$ μm, the EWG R_C remarkably reaches the greatest concentration ratio of approx. 800 at $L_f = 150$ μm. We use the product $TR_c(0, z_f)$ as the WG figure of merit. The EWG's value reaches the optimal case around $L_f = 160$ μm, where it offers both tight x-ray focusing and high transmission. Figure 2(b) illustrates the spatial distribution of $R_c(r, z)$ for Pt-cladding EWG at $L_f = 160\mu$m where the EWG is optimized. The axial dependence defines the intrawaveguide Rayleigh length as the full width half maximum (FWHM) of $R(0, z)$. The EWG $R_c(0, 161\ \mu m) \approx 800$ value is four times that of CWG with the same parameters [see red arrow in Fig. 2(b)].

Nuclear population inversion. In free space ($R_c = 1$), full nuclear population inversion $I_v = 1$ requires unrealistic x-ray intensities, i.e., either tight focusing or very high photon number. In an EWG, the free-space Rabi frequency is enhanced by the maximum factor of $\sqrt{R_c(0, z_f)}$. As demonstrated in Fig. 2, the required input XFEL photon number n_p for achieving nuclear inversion is reduced by a factor of 28 for the EWG and of 14 for the CWG. Based on Eq. (8), three requirements determine the efficiency of a tapering structure: (i) a few-nanometer x-ray focal spot, defined by the radial FWHM of $R_c(r, z_f)$ in the inset of Fig. 2(b), (ii) a long intrawaveguide Rayleigh length, given by the axial FWHM of $R_c(0, z)$ in the inset of Fig. 2(b), and (iii) low photon loss. The focusing spot radius and the Rayleigh length of the EWG are approximately 5 nm and 2 μm, respectively. We denote the volume defined by the product of the focusing spot and the Rayleigh length as the active volume where the nuclear excitation is predominantly taking place. The EWG in Fig. 2(b) supports an active volume containing 10^6 nuclei with particle number density in Table I. Moreover, the EWG can achieve $T = 0.8$ and so fulfill the condition (iii).

We numerically solve Eqs. (1)–(4) and present the full XFEL-nuclear dynamics in Fig. 3. Figure 3(a) demonstrates the propagation of an XFEL pulse through a Pt-cladding EWG of Fig. 2(b) where a ^{57}Fe sample is embedded in 160 μm $\leqslant z \leqslant$ 165 μm. The axial $R_c(0, z)$ shows that the XFEL intensity reaches the maximum when arriving at $z \approx 161$ μm as also predicted by Fig. 2(b). We use the XFEL parameters $n_p = 2.88 \times 10^{11}$, $\sigma = 120$ nm and pulse duration $\tau = 42.5$ fs corresponding to the FWHM $2\sqrt{2\ln 2}\tau = 100$ fs. On this time scale, the ^{57}Fe nuclei are coherently excited by the pulse and become fully inverted in the focal point region. As showed in Fig. 3(b) which considers now the nuclear inversion at the end of the pulse, the XFEL leaves behind an active volume of $\pi \times 3$ nm $\times 3$ nm $\times 1.7$ μm, containing 2.5×10^6 inverted ^{57}Fe nuclei out of 4.1×10^6 totally embedded isotopes. In Figs. 3(c) and 3(d) we show the n_p-dependent maximum I_v of the isotopes ^{133}Ba, ^{57}Fe, ^{187}Os and ^{169}Tm using

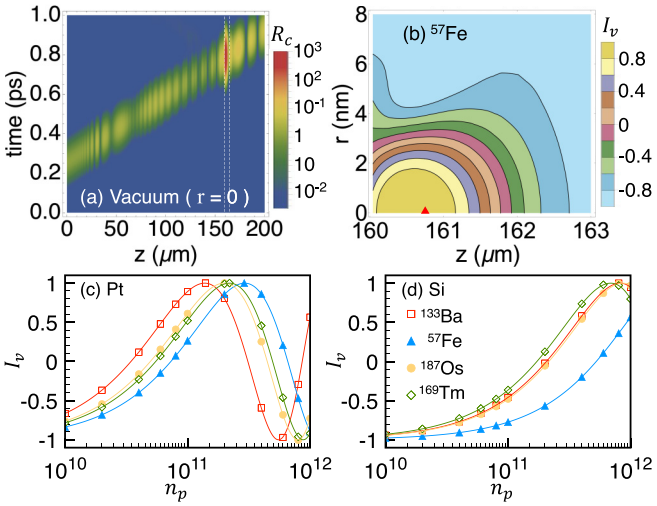

FIG. 3. (a) Axial x-ray $R_c(0, z, t)$ for 14.4 keV x-ray propagation in a Pt-cladding EWG. (b) Spatial distribution of $I_v(r, z)$ driven by a propagating XFEL with $(n_p, \sigma, \tau) = (2.88 \times 10^{11}$, 120 nm, 42.5 fs). The maximum I_v for ^{133}Ba (unfilled red square), ^{57}Fe (filled blue triangle), ^{187}Os (filled yellow circle), and ^{169}Tm (unfilled green diamond) is depicted as a function of the photon number per pulse in a (c) platinum- (d) silicon-cladding EWG. The solid lines are calculated using Eq. (8) with steady-state R_c. $(r_i, L_f, r_o) = (150$ nm, 160 μm, 15 nm) are used for all graphs.

Pt- and Si-cladding EWG, respectively. The numerical results obtained from Eqs. (1)–(4) (points) agree with Eq. (8) for the steady-state value of R_c (solid lines) up to a relative error of less than 0.1%, confirming the validity of the steady-state calculation.

Three conclusions can be drawn based on the results presented in Figs. 3(c) and 3(d). First, all four considered isotopes can be fully inverted around the focus in a Pt-cladding EWG for $10^{11} < n_p < 10^{12}$. Significant inversion occurs also for photon numbers in the range $10^{10} < n_p < 10^{11}$ in a Pt-cladding EWG for ^{133}Ba, ^{187}Os, and ^{169}Tm. Considering the generic figure 10^{12} photons/pulse, our results offer a budget of 1%–10% throughput rate for the required prefocusing. A comparison with predictions in Ref. [31] shows that population inversion in EWG should occur more efficiently and require significantly smaller photon numbers n_p than in x-ray thin-film cavities. Second, the coherent x-ray pulse can drive a Rabi oscillation [66,74]. Third, a comparison between Figs. 3(c) and 3(d) demonstrates that the Pt-cladding EWG provides a better x-ray focusing than the silicon-cladding EWG.

For a more realistic modeling, we have also investigated the effect of surface roughness at the vacuum-cladding interface by introducing random fluctuations of amplitude A_p of the elliptical cladding surface. Glass capillaries have surface roughness of only $0.2 - 0.5$ nm [34], but for other materials A_p can reach several nanometers [75]. Our numerical results in Fig. 4(a) show that the number of inverted nuclei in the focal volume remains $\propto 10^6$ despite increasing A_p from 0 to 10 nm. We also use the partial-coherence method to model SASE XFEL pulses [49] with limited longitudinal coherence times τ_c. As demonstrated in Fig. 4(b), for all nuclear species, the amount of inverted nuclei reaches the 10^5 region when $\tau_c > 10$ fs. The statistics at $\tau_c = 50$ fs shows that 10^6 inverted ^{187}Os, ^{169}Tm, and ^{57}Fe nuclei are already produced by an average of $\langle n_p \rangle \approx 2 \times 10^{11}$ photons per pulse. Fig. 4(c) highlights the realistic region of $\tau_c \leqslant 10$ fs which can be generated by modern seededXFEL [55]. Inverted nuclei numbers on the order of 10^5 are achievable for all considered isotope species. Thus, nuclear inversion is potentially in reach also for just partially coherent XFEL pulses in an EWG.

Discussion. A stronger intensity carries with it more destructive power in the form of heat load. The off-resonant components of the incoming xrays can be decreased by narrow-band monochromatization using $^{57}FeBO_3$ or $^{57}Fe_2O_3$ crystals [9,13,14]. We estimate via Beer's law the heat load on $^{57}FeBO_3$, a canted antiferromagnet, using the pure nuclear reflections on the (111) and (333) crystal planes. Considering an incident XFEL pulse of 2.5 mm beam diameter, 10 meV bandwidth and 10^{11} photons on a cm-size $^{57}FeBO_3$ crystal of 100 μm thickness, a single pulse produces a temperature increase of $\Delta T = 0.08$ K. This temperature increase has a

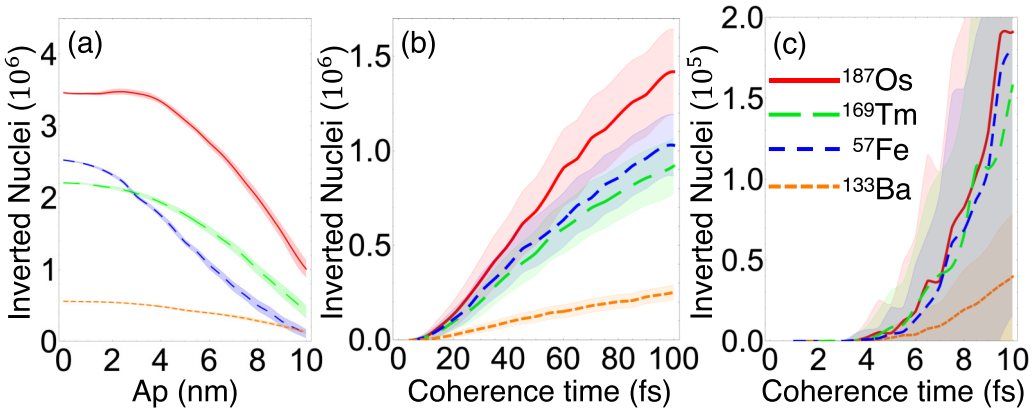

FIG. 4. (a) A_p-dependent number of inverted ^{187}Os (red solid line), ^{169}Tm (green dashed line), ^{57}Fe (blue dotted line), and ^{133}Ba (orange dashed-dotted line) nuclei. The shaded regions depict the error bars averaged over 100 realizations. (b), (c) τ_c-dependent number of inverted nuclei. The XFEL FWHM is 100 fs and $A_p = 0$ for all cases. The shaded regions depict the error bars from 5000 SASE realizations, for illustration purposes scaled by a factor of 0.2. An EWG with $(r_i, L_f, r_o) = (150$ nm, 160 μm, 15 nm) is used for both panels.

negligible effect on the lattice constant according to thermal expansion data of $^{57}FeBO_3$ [76,77] and does not jeopardize the Bragg conditions for the pure nuclear reflections. We note here that our setup does not require and cannot benefit from a large XFEL pulse repetition rate since the nuclear population inversion is achieved in a single shot and decays before the next pulse arrives. Instead, a low XFEL repetition rate, for instance 60 Hz (PAL XFEL [55]), would provide sufficient time between pulses for optimal monochromatization.

Our results demonstrate that x-ray waveguides can increase the radiation intensity by up to three orders of magnitude. An integrated design embedding the nuclear sample directly at the focal area will lead to strong nuclear excitation, accessing the nonlinear effects and nuclear population inversion, a key ingredient for gamma-ray lasers. The successful nuclear population control could be used for depleting nuclear isomers and thus releasing the energy stored therein. A classical example is the 2.4 MeV ^{93m}Mo isomer with 6.8 hours half-life. By driving a 4.8 keV transition upwards to a gateway state, the ground state can be reached in ns [6,78,79]. Our calculations for ^{93m}Mo show that, although nuclear population inversion requires higher photon per pulse than presently available at XFEL facilities, an EWG enhances the achievable excitation by a factor of approximately 200.

Acknowledgments. Y.-H.C., P.-H.L, G.-Y.W., and W.-T.L. are supported by the Ministry of Science and Technology, Taiwan (Grant No. MOST 107-2112-M-008-007-MY3 & MOST 109-2639-M-007-002-ASP & 110-2639-M-007-001-ASP & MOST 110-2112-M-008-027-MY3 & 111-2923-M-008-004-MY3). A.P. gratefully acknowledges support from the Heisenberg Program of the Deutsche Forschungsgemeinschaft (DFG).

[1] P. Emma, R. Akre, J. Arthur, R. Bionta, C. Bostedt, J. Bozek, A. Brachmann, P. Bucksbaum, R. Coffee, F.-J. Decker, Y. Ding, D. Dowell, S. Edstrom, A. Fisher, J. Frisch, S. Gilevich, J. Hastings, G. Hays, Ph. Hering, Z. Huang *et al.*, First lasing and operation of an angstrom-wavelength free-electron laser, Nature Photon **4**, 641 (2010).

[2] C. Pellegrini, A. Marinelli, and S. Reiche, The physics of x-ray free-electron lasers, Rev. Mod. Phys. **88**, 015006 (2016).

[3] B. W. Adams, C. Buth, S. M. Cavaletto, J. Evers, Z. Harman, C. H. Keitel, A. Pálffy, A. Picón, R. Röhlsberger, Y. Rostovtsev, and K. Tamasaku, X-ray quantum optics, J. Mod. Opt. **60**, 2 (2013).

[4] A. I. Chumakov, A. Q. R. Baron, I. Sergueev, C. Strohm, O. Leupold, Y. Shvyd'ko, G. V. Smirnov, R. Rüffer, Y. Inubushi, M. Yabashi *et al.*, Superradiance of an ensemble of nuclei excited by a free electron laser, Nat. Phys. **14**, 261 (2018).

[5] G. C. Baldwin and J. C. Solem, Recoilless gamma-ray lasers, Rev. Mod. Phys. **69**, 1085 (1997).

[6] P. Walker and G. Dracoulis, Energy traps in atomic nuclei, Nature (London) **399**, 35 (1999).

[7] G. V. Smirnov, U. van Bürck, A. I. Chumakov, A. Q. R. Baron, and R. Rüffer, Synchrotron mössbauer source, Phys. Rev. B **55**, 5811 (1997).

[8] V. Potapkin, A. I. Chumakov, G. V. Smirnov, J.-P. Celse, R. Rüffer, C. McCammon, and L. Dubrovinsky, The ^{57}Fe Mössbauer Source at the ESRF, J. Synchrotron Rad. **19**, 559 (2012).

[9] Yu. V. Shvyd'ko, T. Hertrich, U. van Bürck, E. Gerdau, O. Leupold, J. Metge, H. D. Rüter, S. Schwendy, G. V. Smirnov, W. Potzel, and P. Schindelmann, Storage of Nuclear Excitation Energy through Magnetic Switching, Phys. Rev. Lett. **77**, 3232 (1996).

[10] G.-Y. Wang and W.-T. Liao, Generation of Short Hard-X-Ray Pulses of Tailored Duration Using a Mössbauer Source, Phys. Rev. Applied **10**, 014003 (2018).

[11] G. V. Smirnov, U. van Bürck, J. Arthur, S. L. Popov, A. Q. R. Baron, A. I. Chumakov, S. L. Ruby, W. Potzel, and G. S. Brown, Nuclear Exciton Echo Produced by Ultrasound in Forward Scattering of Synchrotron Radiation, Phys. Rev. Lett. **77**, 183 (1996).

[12] F. Vagizov, V. Antonov, Y.V. Radeonychev, R. N. Shakhmuratov, and O. Kocharovskaya, Coherent control of the waveforms of recoilless γ-ray photons, Nature (London) **508**, 80 (2014).

[13] U. van Burck, R. L. Mossbauer, G. V. Smirnov, and H. J. Maurus, Enhanced nuclear resonance scattering in dynamical diffraction of gamma rays, J. Phys. C **13**, 4511 (1980).

[14] E. Gerdau, R. Rüffer, H. Winkler, W. Tolksdorf, C. P. Klages, and J. P. Hannon, Nuclear Bragg Diffraction of Synchrotron Radiation in Yttrium Iron Garnet, Phys. Rev. Lett. **54**, 835 (1985).

[15] E. Gerdau, R. Rüffer, R. Hollatz, and J. P. Hannon, Quantum Beats from Nuclei Excited by Synchrotron Radiation, Phys. Rev. Lett. **57**, 1141 (1986).

[16] U. van Bürck, R. L. Mössbauer, E. Gerdau, R. Rüffer, R. Hollatz, G. V. Smirnov, and J. P. Hannon, Nuclear Bragg Scattering of Synchrotron Radiation with Strong Speedup of Coherent Decay, Measured On Antiferromagnetic $^{57}FeBO_3$, Phys. Rev. Lett. **59**, 355 (1987).

[17] Y. V. Shvyd'ko and U. Van Bürck, Hybrid forms of beat phenomena in nuclear forward scattering of synchrotron radiation, Hyperfine Interact. **123/124**, 511 (1999).

[18] J. P. Hannon and G. T. Trammell, Coherent γ-ray optics, Hyperfine Interact. **123/124**, 127 (1999).

[19] G. V. Smirnov, U. van Bürck, W. Potzel, P. Schindelmann, S. L. Popov, E. Gerdau, Yu. V. Shvyd'ko, H. D. Rüter, and O. Leupold, Propagation of nuclear polaritons through a two-target system: Effect of inversion of targets, Phys. Rev. A **71**, 023804 (2005).

[20] R. Röhlsberger, K. Schlage, B. Sahoo, S. Couet, and R. Rüffer, Collective lamb shift in single-photon superradiance, Science **328**, 1248 (2010).

[21] R. Röhlsberger, H. C. Wille, K. Schlage, and B. Sahoo, Electromagnetically induced transparency with resonant nuclei in a cavity, Nature (London) **482**, 199 (2012).

[22] K. P. Heeg, H.-C. Wille, K. Schlage, T. Guryeva, D. Schumacher, I. Uschmann, K. S. Schulze, B. Marx, T. Kämpfer, G. G. Paulus, R. Röhlsberger, and J. Evers, Vacuum-Assisted Generation and Control of Atomic Coherences at X-Ray Energies, Phys. Rev. Lett. **111**, 073601 (2013).

[23] K. P. Heeg, J. Haber, D. Schumacher, L. Bocklage, H.-C. Wille, K. S. Schulze, R. Loetzsch, I. Uschmann, G. G. Paulus, R. Rüffer, R. Röhlsberger, and J. Evers, Tunable Subluminal Propagation of Narrow-band X-Ray Pulses, Phys. Rev. Lett. **114**, 203601 (2015).

[24] K. P. Heeg, C. Ott, D. Schumacher, H.-C. Wille, R. Röhlsberger, T. Pfeifer, and J. Evers, Interferometric Phase Detection at X-Ray Energies Via Fano Resonance Control, Phys. Rev. Lett. **114**, 207401 (2015).

[25] K. P. Heeg, A. Kaldun, C. Strohm, P. Reiser, C. Ott, R. Subramanian, D. Lentrodt, J. Haber, H.-C. Wille, S. Goerttler, R. Rüffer, C. H. Keitel, R. Röhlsberger, T. Pfeifer, and J. Evers, Spectral narrowing of x-ray pulses for precision spectroscopy with nuclear resonances, Science **357**, 375 (2017).

[26] J. Haber, X. Kong, C. Strohm, S. Willing, J. Gollwitzer, L. Bocklage, R. Rüffer, A. Pálffy, and R. Röhlsberger, Rabi oscillations of x-ray radiation between two nuclear ensembles, Nat. Photonics **11**, 720 (2017).

[27] K. P. Heeg, A. Kaldun, C. Strohm, C. Ott, R. Subramanian, D. Lentrodt, J. Haber, H.-C. Wille, S. Goerttler, R. Rüffer, C H Keitel, R. Röhlsberger, T. Pfeifer, and J. Evers, Coherent x-ray-optical control of nuclear excitons with zeptosecond phase-stability, Nature (London) **590**, 401 (2021).

[28] J. Haber, K. S. Schulze, K. Schlage, R. Loetzsch, L. Bocklage, T. Gurieva, H. Bernhardt, H.-C. Wille, R. Rüffer, I. Uschmann *et al.*, Collective strong coupling of x-rays and nuclei in a nuclear optical lattice, Nat. Photonics **10**, 445 (2016).

[29] Y. V. Shvyd'ko, S. Stoupin, A. Cunsolo, A. H. Said, and X. Huang, High-reflectivity high-resolution x-ray crystal optics with diamonds, Nat. Phys. **6**, 196 (2010).

[30] Y. Shvyd'Ko, S. Stoupin, V. Blank, and S. Terentyev, Near-100% bragg reflectivity of x-rays, Nat. Photonics **5**, 539 (2011).

[31] K. P. Heeg, C. H. Keitel, and J. Evers, Inducing and detecting collective population inversions of mössbauer nuclei, arXiv:1607.04116.

[32] D. H. Bilderback, S. A. Hoffman, and D. J. Thiel, Nanometer spatial resolution achieved in hard imaging and laue diffraction experiments, Science **263**, 201 (1994).

[33] R. Huang and D. H. Bilderback, Single-bounce monocapillaries for focusing synchrotron radiation: Modeling, measurements and theoretical limits, J. Synchrotron Radiat. **13**, 74 (2006).

[34] X. Zeng, F. Duewer, M. Feser, C. Huang, A. Lyon, A. Tkachuk, and W. Yun, Ellipsoidal and parabolic glass capillaries as condensers for x-ray microscopes, Appl. Opt. **47**, 2376 (2008).

[35] C. G. Schroer and B. Lengeler, Focusing Hard X Rays to Nanometer Dimensions by Adiabatically Focusing Lenses, Phys. Rev. Lett. **94**, 054802 (2005).

[36] M.J Zwanenburg, J. H. H Bongaerts, J. F Peters, D. Riese, and J. F van der Veen, Focusing of coherent x-rays in a tapered planar waveguide, Phys. B: Condens. Matter **283**, 285 (2000).

[37] F. Pfeiffer, C. David, M. Burghammer, C. Riekel, and T. Salditt, Two-dimensional x-ray waveguides and point sources, Science **297**, 230 (2002).

[38] A. Jarre, C. Fuhse, C. Ollinger, J. Seeger, R. Tucoulou, and T. Salditt, Two-Dimensional Hard X-Ray Beam Compression by Combined Focusing and Waveguide Optics, Phys. Rev. Lett. **94**, 074801 (2005).

[39] S. P. Krüger, H. Neubauer, M. Bartels, S. Kalbfleisch, K. Giewekemeyer, P. J. Wilbrandt, M. Sprung, and T. Salditt, Sub-10 nm beam confinement by x-ray waveguides: Design, fabrication and characterization of optical properties, J. Synchrotron Radiat. **19**, 227 (2012).

[40] H.-Y. Chen, S. Hoffmann, and T. Salditt, X-ray beam compression by tapered waveguides, Appl. Phys. Lett. **106**, 194105 (2015).

[41] T. Salditt, S. Hoffmann, M. Vassholz, J. Haber, M. Osterhoff, and J. Hilhorst, X-Ray Optics on a Chip: Guiding X Rays in Curved Channels, Phys. Rev. Lett. **115**, 203902 (2015).

[42] S. Hoffmann-Urlaub, P. Höhne, M. Kanbach, and T. Salditt, Advances in fabrication of x-ray waveguides, Microelectron. Eng. **164**, 135 (2016).

[43] E. A. Stern, Z. Kalman, A. Lewis, and K. Lieberman, Simple method for focusing x rays using tapered capillaries, Appl. Opt. **27**, 5135 (1988).

[44] E. I. Denisov, V. I. Glebov, and N. K. Zhevago, Focusing of x-rays using tapered waveguides, Nucl. Instrum. Methods Phys. Res., Sect. A **308**, 400 (1991).

[45] C. Bergemann, H. Keymeulen, and J. F. van der Veen, Focusing X-Ray Beams to Nanometer Dimensions, Phys. Rev. Lett. **91**, 204801 (2003).

[46] A. Iida and K. Hirano, Kirkpatrick-baez optics for a sub-m synchrotron x-ray microbeam and its applications to x-ray analysis, Nucl. Instrum. Methods Phys. Res., Sect. B **114**, 149 (1996).

[47] National nuclear data center, https://www.nndc.bnl.gov/ensdf/.

[48] Lawrence berkeley national laboratory, https://henke.lbl.gov/optical_constants/asf.html.

[49] T. Pfeifer, Y. Jiang, S. Düsterer, R. Moshammer, and J. Ullrich, Partial-coherence method to model experimental free-electron laser pulse statistics, Opt. Lett. **35**, 3441 (2010).

[50] J. Feldhaus, E. L. Saldin, J. R. Schneider, E. A. Schneidmiller, and M. V. Yurkov, Possible application of x-ray optical elements for reducing the spectral bandwidth of an x-ray sase fel, Opt. Commun. **140**, 341 (1997).

[51] J. Amann, W. Berg, V. Blank, F.-J. Decker, Y. Ding, P. Emma, Y. Feng, J. Frisch, D. Fritz, J. Hastings *et al.*, Demonstration of self-seeding in a hard-x-ray free-electron laser, Nat. Photonics **6**, 693 (2012).

[52] S. Serkez, Self-seeding xfels: Operation principle and challenges, Synchrotron Radiation News **29**, 10 (2016).

[53] C. Emma, A. Lutman, M. W. Guetg, J. Krzywinski, A. Marinelli, J. Wu, and C. Pellegrini, Experimental demonstration of fresh bunch self-seeding in an x-ray free electron laser, Appl. Phys. Lett. **110**, 154101 (2017).

[54] I. Inoue, T. Osaka, T. Hara, T. Tanaka, T. Inagaki, T. Fukui, S. Goto, Y. Inubushi, H. Kimura, R. Kinjo *et al.*, Generation of narrow-band x-ray free-electron laser via reflection self-seeding, Nat. Photonics **13**, 319 (2019).

[55] I. Nam *et al.*, High-brightness self-seeded x-ray free-electron laser covering the 3.5 kev to 14.6 kev range, Nat. Photonics **15**, 435 (2021).

[56] K.-J. Kim, Y. Shvyd'ko, and S. Reiche, A Proposal for an X-Ray Free-Electron Laser Oscillator with an Energy-Recovery Linac, Phys. Rev. Lett. **100**, 244802 (2008).

[57] J. Zemella *et al.*, Numerical simulations of an xfelo for the european xfel driven by a spent beam, in *Proceedings of the 32th International Free-Electron Laser Conference* (JACoW, Geneva, Switzerland, 2012), pp. 429.

[58] B. Adams, G. Aeppli, T. Allison, Alfred QR Baron, P. Bucksbaum, A. I. Chumakov, C. Corder, S. P. Cramer, S. DeBeer, Y. Ding *et al.*, Scientific opportunities with an x-ray free-electron laser oscillator, arXiv:1903.09317.

[59] Y. Shvyd'ko, Output coupling from x-ray free-electron laser cavities with intracavity beam splitters, Phys. Rev. Accel. Beams **22**, 100703 (2019).

[60] P. Rauer, I. Bahns, W. Hillert, J. Roßbach, W. Decking, and H. Sinn, Integration of an xfelo at the european xfel facility, in *Proceedings of the 39th International Free-Electron Laser Conference* (JACoW, Geneva, Switzerland, 2019), pp. 62.

[61] G. Marcus, A. Halavanau, Z. Huang, J. Krzywinski, J. MacArthur, R. Margraf, T. Raubenheimer, and D. Zhu, Refractive Guide Switching a Regenerative Amplifier Free-Electron Laser for High Peak and Average Power Hard X Rays, Phys. Rev. Lett. **125**, 254801 (2020).

[62] K. Li, J. Yan, C. Feng, M. Zhang, and H. Deng, High brightness fully coherent x-ray amplifier seeded by a free-electron laser oscillator, Phys. Rev. Accel. Beams **21**, 040702 (2018).

[63] G. Paraskaki, S. Ackermann, B. Faatz, G. Geloni, V. Grattoni, W. Hillert, C. Lechner, M. Mehrjoo, S. Serkez, and T. Tanikawa, Study of a seeded oscillator-amplifier fel, in *39th Free Electron Laser Conf.(FEL'19), Hamburg, Germany, 26-30 August 2019* (JACOW Publishing, Geneva, Switzerland, 2019), pp. 234–237.

[64] M. O. Scully and M. S. Zubairy, *Quantum Optics* (Cambridge University Press, Cambridge, 2006).

[65] G. S. Agarwal, *Quantum Optics* (Cambridge University Press, Cambridge, 2012).

[66] A. Pálffy, J. Evers, and C. H. Keitel, Electric-dipole-forbidden nuclear transitions driven by super-intense laser fields, Phys. Rev. C **77**, 044602 (2008).

[67] W.-T. Liao, A. Pálffy, and C. H. Keitel, Nuclear coherent population transfer with x-ray laser pulses, Phys. Lett. B **705**, 134 (2011).

[68] W.-T. Liao, A. Pálffy, and C. H. Keitel, Coherent Storage and Phase Modulation of Single Hard-X-Ray Photons Using Nuclear Excitons, Phys. Rev. Lett. **109**, 197403 (2012).

[69] Yu. V. Shvyd'ko, U. van Bürck, W. Potzel, P. Schindelmann, E. Gerdau, O. Leupold, J. Metge, H. D. Rüter, and G. V. Smirnov, Hybrid beat in nuclear forward scattering of synchrotron radiation, Phys. Rev. B **57**, 3552 (1998).

[70] C. Fuhse and T. Salditt, Finite-difference field calculations for two-dimensionally confined x-ray waveguides, Appl. Opt. **45**, 4603 (2006).

[71] X. Kong, W.-T. Liao, and A. Pálffy, Field control of single x-ray photons in nuclear forward scattering, New J. Phys. **16**, 013049 (2014).

[72] I. Bukreeva, A. Popov, D. Pelliccia, A. Cedola, S. B. Dabagov, and S. Lagomarsino, Wave-Field Formation in a Hollow X-Ray Waveguide, Phys. Rev. Lett. **97**, 184801 (2006).

[73] W.-T. Liao, A. Pálffy, and C. H. Keitel, Three-beam setup for coherently controlling nuclear-state population, Phys. Rev. C **87**, 054609 (2013).

[74] T. J. Bürvenich, J. Evers, and C. H. Keitel, Nuclear Quantum Optics with X-Ray Laser Pulses, Phys. Rev. Lett. **96**, 142501 (2006).

[75] M. Osterhoff and T. Salditt, Real structure effects in x-ray waveguide optics: The influence of interfacial roughness and refractive index profile on the near-field and far-field distribution, Opt. Commun. **282**, 3250 (2009).

[76] A. Zamkovskaya, E. Maksimova, I. Nauhatsky, and M. Shapoval, X-ray diffraction investigations of the thermal expansion of iron borate $FeBO_3$ crystals, J. Phys.: Conf. Ser. **929**, 012030 (2017).

[77] P. A. Markovin, A. M. Kalashnikova, R. V. Pisarev, and Th. Rasing, Optical study of the electronic structure and magnetic ordering in a weak ferromagnet $FeBO_3$, JETP Lett. **86**, 712 (2008).

[78] J. Gunst, Y. A. Litvinov, C. H. Keitel, and A. Pálffy, Dominant Secondary Nuclear Photoexcitation with the X-Ray Free-Electron Laser, Phys. Rev. Lett. **112**, 082501 (2014).

[79] Y. Wu, J. Gunst, C. H. Keitel, and A. Pálffy, Tailoring Laser-Generated Plasmas for Efficient Nuclear Excitation by Electron Capture, Phys. Rev. Lett. **120**, 052504 (2018).